JOURNAL OF SYNCHROTRON RADIATION

ISSN 1600-5775

Coherent diffractive imaging: towards achieving atomic resolution

S. H. Dietze and O. G. Shpyrko*

Department of Physics and Center for Advanced Nanoscience, University of California, San Diego, La Jolla, CA 92093, USA. *Correspondence e-mail: oleg@physics.ucsd.edu

Received 12 March 2015
Accepted 16 September 2015

Keywords: coherent diffractive imaging; atomic resolution; image quality; necessary dose; signal-to-noise ratio.

The next generation of X-ray sources will feature highly brilliant X-ray beams that will enable the imaging of local nanoscale structures with unprecedented resolution. A general formalism to predict the achievable spatial resolution in coherent diffractive imaging, based solely on diffracted intensities, is provided. The coherent dose necessary to reach atomic resolution depends significantly on the atomic scale structure, where disordered or amorphous materials require roughly three orders of magnitude lower dose compared with the expected scaling of uniform density materials. Additionally, dose reduction for crystalline materials are predicted at certain resolutions based only on their unit-cell dimensions and structure factors.

1. Introduction

X-rays have been used to successfully determine the atomic structure of crystalline materials of increasing complexity for over 100 years. Obtaining the unit cells of simple crystals was one of the first great achievements of X-rays (Bragg, 1913). This method routinely allows the refinement of atomic positions in highly ordered crystals with better than 1 pm precision (Stinton & Evans, 2007; Bell *et al.*, 2009). Furthermore, protein crystallography has obtained the structure of extremely important organic molecules such as DNA (Watson & Crick, 1953) and penicillin (Crowfoot *et al.*, 1949), which have greatly impacted our understanding of life and medicine. However, crystallography only determines the average atomic positions in perfectly periodic crystalline structures. Thus, these methods have not been able to address the materials that cannot be crystallized, the location of defects in crystals, or the atomic positions in disordered materials.

Atomic resolution has been achieved for surfaces using scanning probes (Foster *et al.*, 2001) and for very thin films using transmission electron microscopy (Schweinfest *et al.*, 2001); however, interfaces can differ significantly from the bulk. Since X-rays penetrate bulk materials, have sufficiently short wavelength and have chemical sensitivity, they are ideal for atomic-scale three-dimensional microscopy. Both X-ray full-field imaging and scanning transmission microscopy have had great success (Weiß *et al.*, 2000; Johansson *et al.*, 2007). Although they can still be improved, these techniques can never reach atomic resolution due to their reliance on optical elements (Withers, 2007). Instead of using incoherent radiation to image only ordered materials, it is possible to image any material, up to the diffraction-limited resolution, using coherent X-ray diffractive imaging (CXDI). In order to accomplish this, one must solve for missing phase information in the measured diffraction intensity and back propagate the full complex field to the sample (Fienup, 1980; Miao *et al.*,

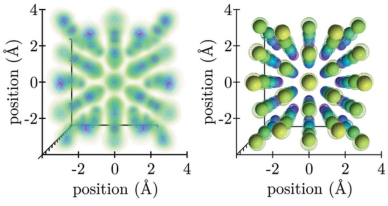

1999). Since the interactions between particles and fields are well understood at the atomic level, a quantitative image of the atomic structure can be formed. The iterative phase retrieval method has rapidly improved and CXDI is now widely used to obtain the local distribution of electron densities and lattice strain of nanocrystals (Newton *et al.*, 2010; Ulvestad *et al.*, 2014; Kim *et al.*, 2014). In addition, CXDI has achieved great success in imaging non-periodic structures (Miao *et al.*, 2006; Chapman *et al.*, 2006; Tripathi *et al.*, 2011).

The necessary dose to image a sample at a particular resolution, δx, has previously been suggested to scale as δx^{-n}, where $n = 4$ or 5 (Shen *et al.*, 2004; Starodub *et al.*, 2008; Howells *et al.*, 2009). This implies that a very large increase in X-ray flux, compared with current available sources, is necessary to reach atomic resolution. We will show that, with increasing disorder, atomic resolution can be achieved at doses well before the power-law scaling predicts. In §2 we will discuss a method to predict the number of photons required to image a particle at a desired resolution. As an example, we generate the atomic positions of two materials, simulate their diffraction pattern at various photon doses and use phase retrieval algorithms to obtain a reconstructed image of the atomic positions. In §4 we show the results of the reconstructions, which validate the predictions made. Finally, in §5 we discuss the performance of currently available X-ray sources and anticipate what next-generation sources in the near future will be able to achieve.

2. Image quality

It is important to understand image quality for any microscope and to predict what can be achieved under various conditions in order to find limiting factors. In this case, we restrict ourselves to images formed from far-field diffraction patterns, such as in CXDI. The far-field kinematic scattering is proportional to the Fourier transform of the electron density, $F(\mathbf{q}) = -(r_0/R)\sum_m f_m \exp(-i\mathbf{q}\cdot\mathbf{r}_m)$, where f_m is the atomic scattering factor of atom m. The expected image resolution can be estimated from the spatial frequency, q_c, where the average signal-to-noise ratio (SNR) drops below some threshold (see Appendix *A* for a detailed derivation of this condition). Here, the resolution refers to the single-pixel resolution, generally thought of as half of the actual resolution. For direct-space imaging a threshold of 5 is common (Burgess, 1999), while for CXDI this threshold is usually set to 1 (Chapman *et al.*, 2006), which is also used here. This condition may be written in terms of the number of photons scattered and collected, $I(q_c)\eta a t \approx [1+(1+4\varsigma^2)^{1/2}]/2 \equiv \Sigma$, where $I(q) = I_0\langle P(\mathbf{q})|F(\mathbf{q})|^2\rangle_q$ is the azimuthally averaged scattered flux, t is the exposure time, a is the area of the detector pixels, η is the detector efficiency, ς is the noise level of the detector, and P is a geometric factor due to polarization of the incoming X-rays. Although this relation is strictly valid only for isotropically scattering samples, it also holds true for scattering from crystalline materials, which have strong Bragg diffraction peaks. This is because the cutoff spatial frequency is limited by regions with low SNR (*i.e.* regions between Bragg peaks), which are relatively uniform.

To meet the oversampling condition needed for CXDI, the area of each detector pixel should be $a = R^2(\lambda/s\Delta x)^2$, where R is the distance from the sample to the pixel, $\lambda \leq 4\delta x$ is the photon wavelength, and s is the one-dimensional oversampling ratio along the maximum size of the sample, Δx. Restricting ourselves to a detector with azimuthal symmetry, such as flat or spherical detectors, the exposure time needed to adequately measure a single slice of Fourier space at the desired single-pixel resolution, $\delta x = \pi/q_c$, is

$$t = \frac{s^2\Sigma}{I_0\eta\lambda^2\upsilon\langle P(\mathbf{q})|\tilde{F}(\mathbf{q})|^2\rangle_{q=q_c}\Delta x}, \qquad (1)$$

where $\tilde{F}(\mathbf{q}) = (R/\sqrt{V})F(\mathbf{q})$ is the normalized scattering factor and $\upsilon \equiv V/\Delta x^3$ is the percent volume fraction of the particle. For unpolarized X-rays, $P(\varphi) = (1/2)(1+\cos^2\varphi)$, which can equivalently be achieved with linear polarization and sufficient rotational freedom of the sample. Here, s represents the oversampling ratio at the spatial frequency corresponding to the desired resolution and must be chosen such that all lower spatial frequencies are sufficiently sampled as well. Thus, flat detectors, which oversample higher frequencies more, will be at a disadvantage to curved detectors that more evenly sample the Ewald sphere.

By using the normalized scattering factor, it is easier to see the general trend in equation (1). The factor $\sqrt{V}$ is necessary to normalize the intensity by the size of the particle. When the correlation length is much smaller than the total size of the particle, such as in amorphous materials or highly disordered crystals, then the overall intensity scales with the number of uncorrelated volumes. Apart from fluctuations in the coherent speckle, which encode the location of each atom, the normalized scattering factor is independent of particle size, in this limit. However, perfect single crystals will not exhibit this simple behavior. Instead, increasing the amount of material redistributes the scattering by narrowing the Bragg peaks, which includes the (000) peak present for all materials. As will be seen later, the normalized scattered flux is then inversely proportional to the size of the particle.

When the scattering angle is small, such that the measured Fourier slice is roughly planar, the data represent a projection of the sample and equation (1) represents the imaging time necessary to distinguish a two-dimensional (2D) pixel of size δx^2 in the projection with statistical significance. In order to extend this to three dimensions, the contribution of a three-dimensional voxel in the sample must provide statistically significant information in the projection. If the sample is roughly uniform, the scattering from a single slice of thickness δx gives the appropriate voxel contribution. Since oversampling must be maintained, the flux should be distributed between $s\Delta x/\delta x$ such slices and multiplying equation (1) by this factor gives the condition to obtain the three-dimensional (3D) resolution, δx^3. By extension, it would also be the condition to obtain the same voxel resolution from the set of tomographic projections necessary to obtain the full 3D

spatial information, using dose fractionation (Hegerl & Hoppe, 1976; McEwen *et al.*, 1995).

It is possible to obtain a similar, more general, result by considering taking a series of 2D slices, each satisfying equation (1). To sample the 3D Fourier space, the sample must be rotated perpendicular to the incoming radiation direction while oversampling all voxels up to the largest spatial frequency needed for a particular resolution. To evenly sample the entire Ewald sphere at the maximum spatial frequency, a sample could be rotated in all possible directions with a solid angle of $\delta\Omega = (\delta q/q_c)^2$, thus requiring $N = \pi(s\Delta x/\delta x)^2$ slices. However, since each slice has $n = ks\Delta x \sin(\varphi_m)$ sampling points at the maximum spatial frequency, where $\varphi_m = 2\arcsin(\lambda/4\delta x)$ is the maximum necessary scattering angle and $k = 2\pi/\lambda$ is the wavenumber, the time spent at each rotation angle should be normalized such that all voxels at the maximum spatial frequency are only sampled a total time of t. The oversampling ratio introduced by rotation can be set independently of the detector oversampling, but for simplicity we will let them be the same. The total exposure time is then given by

$$\frac{N}{n}t = \frac{s^3\Sigma}{I_0\eta\lambda^2\upsilon\left\langle P(\mathbf{q})|\tilde{F}(\mathbf{q})|^2\right\rangle_{q=q_c}\delta x}\,\frac{2\sin(\varphi_m/2)}{\sin(\varphi_m)}. \qquad (2)$$

For small-angle scattering, where the maximum necessary scattering angle is small, the normalized number of slices reduces to $N/n = s\Delta x/\delta x$ and the total exposure time is the same result as expected from dose fractionation.

The total exposure time needed can be reduced by increasing the available flux or by making use of scattering resonances. Additionally, it is not strongly dependent on the sample size because any gain in scattered intensity due to more material is negated by the additional sampling required. In practice, however, it will be easier to image smaller samples with the use of focusing to achieve a higher X-ray flux. Furthermore, using a wavelength nearly three and a half times the resolution desired and obtaining scattering in a good amount of the full 4π solid angle can reduce the required sampling time, as long as the atomic scattering factors do not drastically reduce with lower energies.

It is important to note that flat detectors are exclusively used in X-ray science, thus far. Such detectors unevenly sample a Fourier slice when scattering angles become large. Resampling the data will introduce further noise at high spatial frequencies, further increasing the expected sampling time to achieve a particular resolution. In addition, the maximum scattering angle is significantly more restricted. With an optimal maximum scattering angle near $\pi/4$, the potential benefits in dose reduction due to increasing wavelength are decreased as compared with curved detectors.

Since it is not always possible to set the desired oversampling ratio during the measurement, the data may later be binned to obtain a lower oversampling ratio. The necessary sampling time [equations (1) and (2)] will remain correct, with the new oversampling ratio and the detector noise adjusted for the number of pixels binned together, $\varsigma' = (\sum_j \varsigma_j^2)^{1/2}$. In addition, when measuring highly asymmetrical samples where the percent volume fraction is small, it is possible to bin data along one or two dimensions, as appropriate, to reduce the necessary sampling time.

It is not practical to rotate the sample through all possible orientations. Instead, it is more likely that the sample will be rotated about a single axis only. When this is done, some voxels at the maximum spatial frequency are unnecessarily sampled too much. In addition, other spatial frequencies may not be sampled at all due to limits in rotation angle, sweeping of the Ewald sphere when the maximum scattering angle is large, and necessity to block the direct beam. This reduces the expected resolution; thus, equation (2) represents a minimum necessary total sampling time. In some cases, the missing data can be overcome by additional information such as constraints on the set (Thibault *et al.*, 2006) or redundancy from overlapping projections such as in ptychography (Tripathi *et al.*, 2011). In addition, away from resonances the scattering factors are primarily real and the scattered intensity becomes centrosymmetric, which can be used to fill in missing information or to increase SNR (Takahashi *et al.*, 2009).

To consider the general trend of equation (2), take for instance a uniform spherical particle whose scattering factor is proportional to $j_1(q\Delta x)(q\Delta x)^{-1}$, where $j_1(q\Delta x)$ is the spherical Bessel function of the first kind. Since we are interested in resolutions much smaller than the particle itself, we can consider the limiting case $q\Delta x \gg 1$. In this case the scattering intensity due to the particle form factor decays as q^{-4}. Using equation (2) we see that for a uniform density particle the total time needed to image a particle would be $(N/n)\,t \propto \delta x^{-5}$. This assessment is discouraging, since reaching atomic resolution for even high-Z materials would require of the order of 10^5 improvement in average flux, which will not be feasible for any X-ray source within the next few decades. Fortunately, as we will see in §4, this is not the case because the particle is in fact made of discrete objects, resulting in order at the atomic scale.

3. Method

We created the atomic positions of two particle types. First, a crystalline Au particle was created using the known face-centered cubic unit-cell parameters (Jette & Foote, 1935). Several defects were introduced, including one screw dislocation of nominal width 5 Å with slip plane (111) and Burger's vector $[1\bar{1}0]\,a/2$. Additionally, two vacancies and two interstitials, with local distortion size of 5 Å, were added. The particle was shaped into an asymmetric spheroid with nominal diameter of 20 nm, containing 2×10^5 atoms. Secondly, an amorphous Au particle was created using the ideal amorphous solid model with hard spheres (Lee *et al.*, 2010). First, a single atom is generated and $4 \leq l \leq 12$ atoms distributed randomly around it, such that they are all 'touching' the central atom. This cluster forms a seed, upon which further atoms are added without violating minimum interatomic distances. The number of atoms in the seed strongly influences the final packing ratio of the particle generated. Here we use $l = 9$ resulting in a packing ratio of 0.60. The amorphous Au particle, like the

crystalline particle, consists of 2×10^5 atoms and is the same size and shape.

Once we had the positions of all atoms [Fig. 1(*a*)], we simulated diffraction data by performing an explicit Fourier transform (FT) onto a regular Cartesian 3D grid [Fig. 1(*b*)]. For each atom type in the particle the FT is performed separately and scaled using an estimated q-dependent scattering factor and Debye–Waller factor at 10 keV photon energy near room temperature (Waasmaier & Kirfel, 1995; Peng *et al.*, 1996). Although we have ignored higher-order thermal diffuse scattering (TDS) beyond the Debye–Waller factor, its contribution can be significant for low-Z materials when approaching the Debye temperature (Als-Nielsen & McMorrow, 2011). TDS will contribute an incoherent background to the scattering intensity due to phonons in the material. This can become a significant problem in regions of low coherent scattering, such as between Bragg peaks in highly ordered crystalline materials. Since CXDI is optimal for relatively small particles, of the order of a few hundred nanometers or less, the error introduced by TDS is expected to be minimal for materials like Au at room temperature. However, there will be many cases where TDS will need to be subtracted by using other measurements, theoretical predictions or approximately by observing loss in coherent speckle visibility (Wu *et al.*, 1999; Holt *et al.*, 1999).

Since the grid oversamples the diffraction pattern it is smoothly varying between neighboring voxels on the grid, and the diffraction intensity was calculated only for the center of each voxel and not integrated over the entire voxel volume. Actual measured data will be a recombined series of 2D slices. To achieve appropriate oversampling at large spatial frequencies during rotation of the sample, small spatial frequencies will be oversampled much more. We simply counted the number of times each voxel on the 3D grid would be sampled assuming a curved detector and independent two-axis rotation. These counts are multiplied to our simulated 3D diffraction pattern before applying Poisson statistics. This circumvents the extremely costly technique of simulating a series of 2D diffraction patterns and then mapping those pixels to the 3D Cartesian grid. Since interpolation (Rasche *et al.*, 1999) is used to map the data, which is affected by the instrument resolution function (Sinha *et al.*, 1998; Song *et al.*, 2007), additional errors will be introduced in measurements. Alternatively, a cylindrical grid can be used, which more accurately represents the measured sampling, in conjunction with the fast polar-FT (Averbuch *et al.*, 2006; Fenn *et al.*, 2007) for phase retrieval. However, this is significantly more computationally costly due to the ill-defined inverse polar transform and very memory intensive due to the storage of the highly over-sampled data near the origin.

To illustrate the minimum error that is introduced by discretizing the diffraction data, the electron density is obtained by performing the inverse fast Fourier transform (FFT) of the simulated full complex diffraction data [Fig. 1(*c*)]. Since no effort was made to match voxel positions with atom positions, the recovered electron density for each atom location extends beyond a single pixel. However, finding local maxima in the electron density combined with subpixel shifts allows us to recover the approximate location of the atoms and their atomic number [Fig. 1(*d*)]. The recovered locations have a mean absolute error (MAE), $(1/N)\sum_j^N ||\mathbf{r}_j - \mathbf{r}'_j||$, and maximal error (ME), $\max_{j\in[N]} ||\mathbf{r}_j - \mathbf{r}'_j||$, of 0.12 Å and 0.22 Å, respectively, which is far below the voxel size used of 0.78 Å.

Reconstruction of the electron density from simulated diffraction intensities is carried out using the hybrid input–output (HIO) algorithm (Fienup, 1982) and difference map (DM) algorithm (Elser, 2003). The only real space constraint used is a support, which defines the approximate particle's shape, that is allowed to change through the shrinkwrap method (Marchesini *et al.*, 2003*b*). Although it is possible to start the recovery from a completely random guess, recovering a set of discrete objects is notoriously time-consuming. The reconstruction process essentially traverses randomly through a very large phase space until it comes close to the solution (Elser, 2003). Since the efficacy of phase retrieval algorithms has already been vetted (Marchesini *et al.*, 2003*a*; Quiney, 2010; Miao *et al.*, 2015) and it is known that only trivial ambiguities in the solution exist under appropriate conditions (Bates, 1984), it is not necessary to start with completely random guesses to determine the achievable resolution. It is only necessary to not bias any particular stagnation point or near solution point of the noisy data. To reduce the number of total iterations needed, we start the reconstructions with a linear combination of the actual solution and random complex

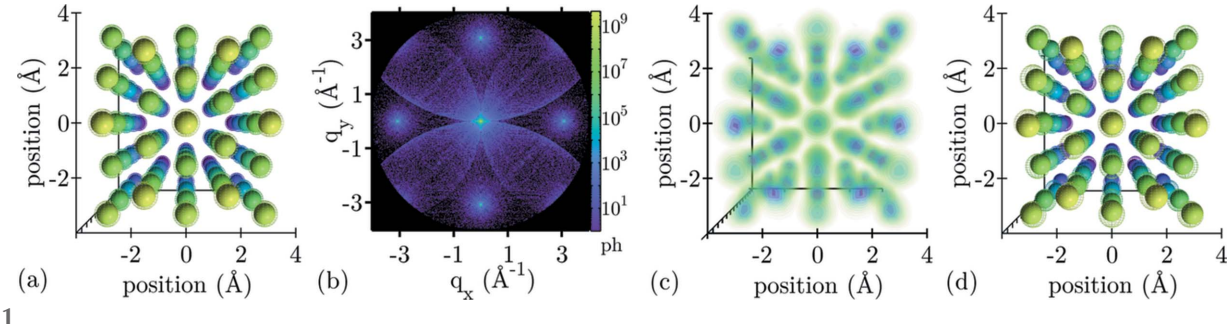

Figure 1
Method of simulation. (*a*) Atomic positions are generated (color is used to better indicate depth), which are (*b*) Fourier transformed to a regular Cartesian 3D grid (scattered photons shown on log scale). (*c*) An inverse fast Fourier transform of the full complex scattered wave gives the electron density from which (*d*) the atomic positions and atomic number (indicated by size) can be recovered. Dashed spheres designate the actual atomic positions for comparison.

values within the support. The actual solution is first randomly sub-pixel shifted and convolved with a Gaussian point spread function (PSF). To reduce the chance of bias, the PSF is chosen with a full width at half-maximum greater than the final image resolution and the random values allowed to vary of the order of the maximum electron density. The initial support is obtained from a reconstruction of the low-frequency data, but can also be acquired by an autocorrelation (Crimmins *et al.*, 1990) or use of locator sets (Fienup *et al.*, 1997). At least some reconstructions were also started with just the noise inside of the support and agree with reconstructions from the better initial guesses. An average reconstruction is formed by combining the best 11 of 15 total reconstructions after adjusting for any trivial ambiguities such as constant phase offset, relative particle translation, and the complex conjugated mirror image. From this, the mean absolute error (MAE) between the recovered and actual phase of the diffraction pattern is calculated and averaged azimuthally along shells of constant $|\mathbf{q}|$, $(2/\pi)\langle||\theta'(\mathbf{q}) - \theta(\mathbf{q}) : \theta' - \theta \in (-\pi, \pi]||\rangle_q$. Here, the MAE is normalized such that a value of 0 would be a perfect correlation between measured and recovered, 2 is a perfect anti-correlation (*i.e.* π phase shift), and 1 is equal correlation and anti-correlation or no correlation at all. We defined the single-pixel resolution of the recovered electron density as π/q_c, where q_c is the lowest spatial frequency where the MAE becomes greater than 0.5. This is equivalent to the phase retrieval transfer function (PRTF) commonly used to define resolution when the solution is not known, except that the PRTF measures how well the set of solutions compare with each other instead of a known solution (Chapman *et al.*, 2006; Tripathi *et al.*, 2011). Thus, if the recovered solutions always stagnate in the same local minima during phase retrieval, the PRTF will indicate a better resolution than actually achieved. We use the PRTF to check that we have not biased our solutions with the given starting guesses.

4. Results and discussion

To test the predictions of equation (2), we have simulated the diffraction data for several materials and used CXDI to reconstruct their atomic position. For this, we assume a photon energy $E = 10$ keV, a perfect photon capture efficiency of the detector $\eta = 1$, and no detector noise $\varsigma = 0$. Here we use a one-dimensional oversampling $s = 2$, which is sufficient to achieve high probability of reconstruction success but in some cases can be lower (Miao *et al.*, 1998).

The crystalline Au diffraction intensity was simulated with a wide range of time-integrated photon flux (TIPF) between 6×10^{14} photons μm^{-2} and 1×10^{19} photons μm^{-2}. The resolution obtained using CXDI of these simulations matches extremely well to the predictions from equation (2) until the expected resolution becomes lower than the pixel size.[1] The resolution *versus* TIPF initially follows a power law decay proportional to δx^{-5} [Fig. 2(*a*)], as expected. This power law decay would continue forever for scattering from a sample with uniform electron density. However, for a sample with correlations, in this case long-range order producing Bragg peaks, the cutoff frequency that determines resolution will jump across the regions of increased SNR, as indicated by the sharp drop at 1×10^{18} photons μm^{-2} in Fig. 2(*a*), for instance. The resolution at which this curve becomes discontinuous is directly tied to the spatial frequencies of the Bragg peaks. Additionally, the size of the jumps will depend primarily on the relative intensity of the Bragg peaks. From the expected q^{-4} fall-off of the intensity away from the Bragg peaks, we can estimate the start of the jump by the spatial frequencies where the azimuthally averaged intensity between two Bragg peaks is at its minima. The start of the first jump (derived in Appendix *B*) is

$$q_1 \approx \frac{q_b}{2}\left(\frac{40\rho + 1}{30\rho + 1}\right), \tag{3}$$

where $\rho = |F_{(000)}|^2/m_b|F_b|^2$ is the ratio of intensity from the (000) Bragg peak and the lowest non-forbidden reflections at q_b, with multiplicity of m_b due to symmetry. Since the intensities can be obtained from the structure and atomic form factor, this can be calculated *a priori* for known structures. The end of the jump will be given by

$$q_2 \approx \frac{18}{11}\, q_b - \frac{5}{8}\, q_1. \tag{4}$$

Although the Bragg peaks become more narrow with larger particle size, it does not modify the start and end location of the jump. The reduction in TIPF to reach atomic resolution is thus always the same, albeit the absolute TIPF changes.

For crystalline Au, the first jump is due to the {111} Bragg peaks at $q_{111} = 2.67$ Å^{-1} with $\rho \approx 0.177$. Thus, $q_1 \approx 1.7$ Å^{-1} and $q_2 \approx 3.3$ Å^{-1}. In other words, we expect a jump once we reach approximately 1.9 Å resolution and jump to approximately 0.95 Å resolution. As also observed in Fig. 2(*a*), this jump results in a factor of 30 reduction in TIPF to reach atomic resolution as compared with the power law decay.

Since achievable resolution from equation (2) and from simulated results are a measure of the average resolution, we show the local resolution of a recovered vacancy and screw dislocation compared with known atomic positions. The known vacancy, as viewed from the [110] direction, is missing a central atom and distorts a small neighborhood of atoms around it [Fig. 2(*b*)]. At 2×10^{18} photons μm^{-2} the vacancy is fully recovered, including the full neighboring distortion [Fig. 2(*c*)]. The MAE and ME are within recoverable atom position limits [Fig. 2(*a*)]. At 1.5×10^{18} photons μm^{-2} the vacancy is still seen [Fig. 2(*d*)]. The central atom is missing as expected but the distortion of neighboring atoms is incomplete. Finally, the vacancy is not recovered for 10^{18} photons μm^{-2} [Fig. 2(*e*)]. Only a very slight distortion from the perfectly periodic lattice is recovered. The screw dislocation when viewed from the [111] direction appears as a continuous shift of atoms from one unit cell to the next [Fig. 2(*f*)]. At $2 \times$

[1] Since the diffraction data are obtained by rotating the sample along two independent axes, the normalized number of slices in equation (2) is modified accordingly, increasing the necessary dose by approximately a factor of four compared with the absolute minimum.

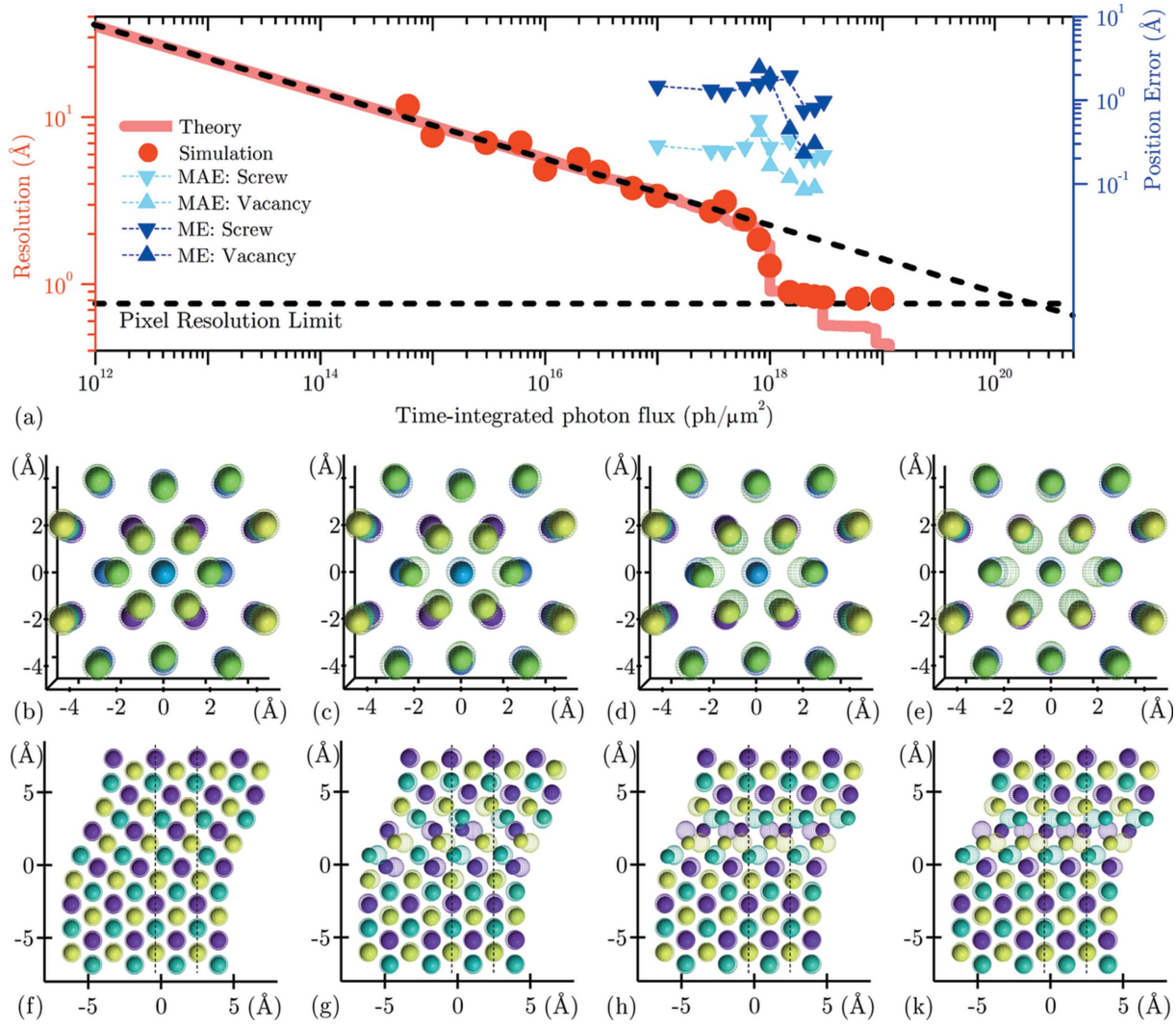

Figure 2
Crystalline Au particle. (*a*) Achievable resolution at various photon statistics, where the solid line is the theoretical model described by equation (2) and circles are reconstructions using CXDI from simulated photon statistics. The horizontal dashed line indicates the pixel size below which the current simulations cannot reach, and the dashed line which follows much of the theoretical curve indicates the expected δx^{-5} fall-off for a uniform particle. To show local resolution, a subset of recovered atomic positions near a vacancy (*b*)–(*e*) and near a screw dislocation (*f*)–(*k*) are shown, where atomic position ME and MAE (*a*) are also given. (*b*) For the actual atomic position near a vacancy there is an atom missing at the center surrounded by an inward distortion of neighboring atoms within 5 Å. (*c*) This is fully recovered by 2×10^{18} photons μm^{-2}. (*d*) With 1.5×10^{18} photons μm^{-2} the vacancy and distortion can still be identified. (*e*) By 10^{18} photons μm^{-2} the vacancy is no longer present and only a slight distortion of neighboring atoms is seen. (*f*) For the actual atomic position near a screw dislocation, a shift of atoms by a unit cell occurs as seen from the [111] direction with characteristic width of 5 Å. (*g*) This is effectively recovered by 2×10^{18} photons μm^{-2} within the expected resolution. (*h*) With 4×10^{17} photons μm^{-2} the dislocation can still be recognized. (*k*) Finally, at 10^{17} photons μm^{-2}, only a periodic atomic structure is recovered. The dashed spheres designate the actual atomic positions for comparison.

10^{18} photons μm^{-2} this shift is fully recovered within the pixel resolution [Fig. 2(*g*)]. At 4×10^{17} photons μm^{-2} the screw dislocation can be recognized due to its spatial extent, but the atomic positions are not correct [Fig. 2(*h*)]. Finally, at 1×10^{17} photons μm^{-2}, the dislocation can no longer be seen and an almost perfectly periodic structure is recovered [Fig. 2(*k*)].

Similarly, the amorphous Au diffraction intensity was simulated with a wide range of TIPF between 3×10^{14} photons μm^{-2} and 1×10^{18} photons μm^{-2}. Again, the resolution obtained using CXDI of these simulations matches very well to the predicted resolution from equation (2) until the expected resolution becomes lower than the pixel size. Below approximately 1×10^{16} photons μm^{-2} the result is identical to crystalline Au, following the δx^{-5} power law decay, since the average electron density is the same for both above 5 Å resolution [Fig. 3(*a*)]. Similar to crystalline Au, amorphous Au exhibits a discontinuity in resolution compared with TIPF because of short-range atomic order resulting in a broad peak in the liquid structure factor. Although the exact discontinuity cannot be determined theoretically, the first jump will be in the vicinity of the closest interatomic distance and will be significantly larger compared with the crystalline case. For amorphous Au, a jump from 3 Å to the resolution limit of 0.78 Å occurred at 1×10^{17} photons μm^{-2}. The jump

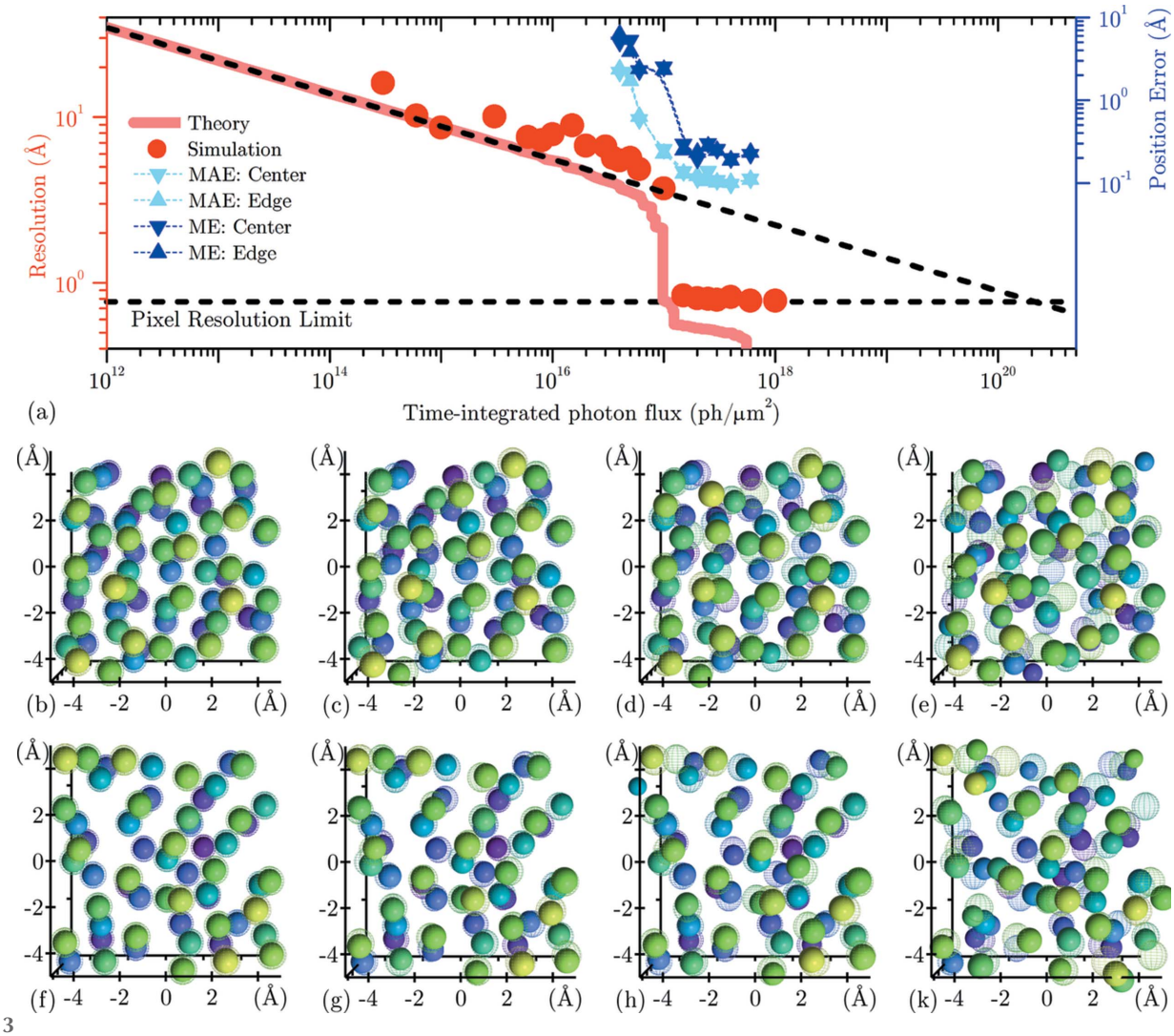

Figure 3
Amorphous Au particle. (*a*) Achievable resolution for various photon statistics, where the solid line is the theoretical model described by equation (2) and circles are reconstructions using CXDI from simulated photon statistics. The horizontal dashed line indicates the pixel size below which the current simulations cannot reach, and the dashed line which follows much of the theoretical curve indicates the expected δx^{-5} fall-off for a uniform particle. To show local resolution, a subset of recovered atomic positions at the center (*b*)–(*e*) and edge (*f*)–(*k*) of the particle are shown, where atomic position ME and MAE (*a*) are also given. The actual atomic position at the center (*b*) and edge (*f*) of the particle are fully recovered by 1.5×10^{17} photons μm^{-2} (*c*) and (*g*). At 10^{17} photons μm^{-2} (*d*) and (*h*), all but one atom matches the known solution for the center and edge, respectively. Finally, at 6×10^{16} photons μm^{-2} (*e*) and (*k*) a large number of atomic positions are incorrect.

results in a three orders of magnitude reduction in TIPF to reach atomic resolution as compared with the power law decay.

Again, we show local resolution of the recovered particle, this time at its center and at the top edge. The actual atomic positions [Figs. 3(*b*) and 3(*f*)] are fully recovered by 1.5×10^{17} photons μm^{-2} [Figs. 3(*c*) and 3(*g*)]. At 10^{17} photons μm^{-2} [Figs. 3(*d*) and 3(*h*)] all but one atom matches the known solution in both the center and edge region. Finally, at 6×10^{16} photons μm^{-2} [Figs. 3(*e*) and 3(*k*)] a large number of atomic positions are incorrect. The ME [Fig. 3(*a*)] shows a clear discontinuity at 1×10^{17} photons μm^{-2}, just as predicted by equation (2).

Although the exact expected resolution is dependent on the material used, some generalizations can be made since interatomic distances are similar for all solids. First, the major difference between materials will be the overall electron density, where the X-ray scattering intensity is proportional to its square. For instance, aluminium (Al), which has a very similar structure to crystalline Au, will simply shift the required TIPF at any resolution, in this case an increase by a factor of approximately 40. Biological systems will require even more: roughly three orders of magnitude as compared with Au.

A very important change in the scattering is due to the arrangement of the atoms themselves. As has already been discussed, the disorder of amorphous materials spreads scattering in Fourier space, allowing a distinct advantage in achieving sufficient SNR for all required spatial frequencies. Real materials will fall between the case of a perfect crystal and ideal amorphous solid, which have been used as examples to illustrate their difference.

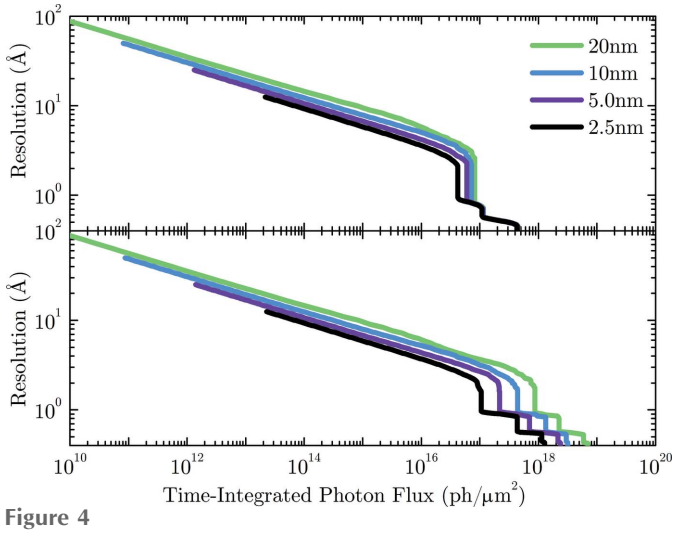

Figure 4
Particle size dependence. Theoretical attainable resolution for amorphous Au particles (top panel) and crystalline Au particles (bottom panel) of different sizes: 20 nm (green), 10 nm (blue), 5 nm (purple) and 2.5 nm (black). Amorphous and crystalline Au are identical for resolutions greater than approximately 5 Å, where the required TIPF is linearly proportional to particle size. Below atomic resolution the required TIPF becomes independent of size for amorphous particles.

Another important change in scattering will occur due the finite size of the particle. Although the additional scattering due to more material will be exactly canceled due to additional sampling required for larger particles, the scattering distribution is also slightly modified with particle size (Fig. 4). As the particle size increases, Bragg peaks become more narrow. Thus, larger particles will generally require more TIPF to achieve the same resolution. The arrangement of atoms is unimportant for resolutions significantly greater than the atomic scale, where the TIPF is observed to be directly proportional to particle size. However, below atomic resolution, while the TIPF for crystalline materials remains approximately linearly dependent on particle size, the TIPF for amorphous materials becomes independent of particle size. Thus, the relative reduction in TIPF when reaching atomic resolution becomes greater for larger amorphous particles and is independent of particle size for crystalline materials, as was predicted (Appendix *B*). In the limit of small particle size, the crystalline and amorphous case become identical.

5. Conclusion

The realization of true atomic resolution using CXDI will require a number of technical problems to be resolved, including high-dynamic-range detectors with high quantum efficiency and low dead-time to reduce waste of illuminating photons. Possibly the most challenging and costly requirement is to obtain sufficiently brilliant X-ray sources to perform experiments within reasonable time periods. Current third-generation sources such as APS, SPring-8, NSLS II and Petra III have a brilliance of (5×10^{13} to 2×10^{15}) photons s^{-1} μm^{-2} $mrad^{-2}$ (0.1% bandwidth)$^{-1}$ near 10 keV (Bilderback *et al.*, 2010). Estimates of usable coherent flux suggest that these sources require of the order of one year of measuring to reach atomic resolution for materials with high electron density. As an example, one of the best 2D resolutions achieved thus far is 3 nm for a silver cube using 1×10^{13} photons μm^{-2} (Takahashi *et al.*, 2009). Adjusting for oversampling, electron density, photon energy and volume fraction, an ideal measurement on a 100 nm gold sphere could have achieved a 2D resolution of 1.1 nm or a 3D resolution of 3.8 nm using the same TIPF. This falls in line with predictions made by equations (1) and (2). Next-generation sources, such as the proposed multi-bend achromat synchrotron and energy-recovery linac, will provide roughly two orders of magnitude increase in brilliance (Eriksson *et al.*, 2008). This makes achieving atomic resolution a real possibility under ideal conditions for radiation-hard samples. The necessity to increase the brilliance of X-ray sources can be alleviated by using partially incoherent radiation for CXDI to increase the usable photons (Thibault & Menzel, 2013; Abbey *et al.*, 2011). Even when full atomic resolution cannot be achieved, order within the particle can lower the flux requirement compared with the simple expected power law decay of an equivalent uniform sample. For instance, crystals with large unit cells produce Bragg peaks at low spatial frequencies (Shirage *et al.*, 2013), which can help to image defects on the length scale of the unit cell. We remark that this method of analysis is valid for any material, including organic samples that cannot be crystallized, which may one day be imaged using fast probes (Neutze *et al.*, 2000).

APPENDIX *A*
Condition of adequate signal-to-noise

We make use of the Shannon sampling theorem, which states that a band-limited signal can be accurately described when sampled at the Nyquist rate (Shannon, 1949; Nyquist, 1928). In other words, if a power spectrum is measured only up to some maximum frequency, q_c, the best expected average image resolution is $\delta x = \pi/q_c$. Strictly speaking, with the use of a discrete Fourier transform, this will be the pixel size. In order to separate two nearby objects, it is required that they are separated by at least two pixels, so the true image resolution may be thought of as twice the pixel resolution. Resolution numbers in this paper refer to the pixel size that adequately describes the signal of a band-limited Fourier spectrum. Although the diffraction of real objects is never truly band-limited, the power spectrum rapidly decreases for larger frequencies and a frequency cutoff can be defined for which higher frequencies can no longer be measured reliably within some noise.

In this case we are not interested in an observer's ability to discern between a signal and noise and thus do not use signal detection theory (Peterson *et al.*, 1954) or the useful simplification of the Rose model (Rose, 1948). Instead, we are only interested in the spatial frequency where noise significantly alters the power spectrum. In that respect we look at the SNR averaged over shells of constant q,

$$\langle \mathrm{SNR}(\mathbf{q})\rangle_q = \left\langle \frac{\mu(\mathbf{q})}{\sigma(\mathbf{q})}\right\rangle_q \equiv \frac{1}{4\pi}\int \mathrm{d}\Omega\, \frac{\mu(\mathbf{q})}{\sigma(\mathbf{q})}. \quad (5)$$

Although most materials are sufficiently isotropic to consider the azimuthal average only, it is possible to define the SNR and spatial resolution along any direction independently. By signal we mean the expected photons scattered from the object of interest captured by a detector of size a with quantum efficiency η during time t, $\mu(\mathbf{q}) = I(\mathbf{q})\eta a t$. This signal, sometimes referred to as contrast, excludes photons directly from the illumination function, sometimes referred to as unscattered photons in the language of the Born approximation. For CXDI, the object is illuminated approximately by a plane wave, which leads to unscattered photons only near $q = 0$. This is different from traditional microscopy, where the measured photons across the entire image can have a significant contribution from photons that do not contribute to the image signal contrast. The total noise, $\sigma(\mathbf{q}) = [\mu(\mathbf{q}) + \varsigma^2]^{1/2}$, is due to the Poisson statistics of photon shot noise and additional noise introduced by the detector, ς. In the limiting case that $\varsigma^2 \ll \mu(\mathbf{q})$ then $\langle \mathrm{SNR}(\mathbf{q})\rangle_q \approx \langle\sqrt{\mu(\mathbf{q})}\rangle_q$, the average scattered photon amplitude. In the other case, when $\varsigma^2 \gg \mu(\mathbf{q})$, $\langle \mathrm{SNR}(\mathbf{q})\rangle_q \approx \langle\mu(\mathbf{q})\rangle_q/\varsigma$. To continue further, we must assume that the sample scatters photons relatively isotropically, such that variations in $\mu(\mathbf{q})$ are small for constant q. Later, we will see that this is not strictly necessary. The averaged SNR is then

$$\begin{aligned}\left\langle \mathrm{SNR}(\mathbf{q})\right\rangle_q &\approx \frac{\left\langle\mu(\mathbf{q})\right\rangle_q}{\left\langle\sigma(\mathbf{q})\right\rangle_q} \\ &= \frac{\left\langle\mu(\mathbf{q})\right\rangle_q}{\left[\left\langle\mu(\mathbf{q})\right\rangle_q + \varsigma^2\right]^{1/2}} \\ &\quad\times \left\{\left\langle\left[1 + \frac{\mu(\mathbf{q}) - \left\langle\mu(\mathbf{q})\right\rangle_q}{\left\langle\mu(\mathbf{q})\right\rangle_q + \varsigma^2}\right]^{1/2}\right\rangle_q\right\}^{-1}. \quad (6)\end{aligned}$$

As we have already assumed, the variations in $\mu(q)$ are small; thus, $[\mu(\mathbf{q}) - \langle\mu(\mathbf{q})\rangle_q]/\langle\mu(\mathbf{q})\rangle_q$ is also small and we may expand this term to first order to find

$$\begin{aligned}\left\langle \mathrm{SNR}(\mathbf{q})\right\rangle_q &\approx \frac{\left\langle\mu(\mathbf{q})\right\rangle_q}{\left[\left\langle\mu(\mathbf{q})\right\rangle_q + \varsigma^2\right]^{1/2}}\left[1 + \frac{1}{2}\left\langle\frac{\mu(\mathbf{q}) - \left\langle\mu(\mathbf{q})\right\rangle_q}{\left\langle\mu(\mathbf{q})\right\rangle_q + \varsigma^2}\right\rangle_q\right]^{-1} \\ &= \frac{\left\langle\mu(\mathbf{q})\right\rangle_q}{\left[\left\langle\mu(\mathbf{q})\right\rangle_q + \varsigma^2\right]^{1/2}}. \quad (7)\end{aligned}$$

We are interested in the maximum spatial frequency, q_c, for which the average SNR is above some threshold, γ, for all $q \le q_c$. Using (7), this condition is

$$\left\langle I(\mathbf{q})\right\rangle_{q\le q_c}\eta a t \;\ge\; \frac{\gamma^2}{2}\left[1 + \left(1 + 4\,\frac{\varsigma^2}{\gamma^2}\right)^{1/2}\right]. \quad (8)$$

Since we are interested in the smallest spatial frequency where the average SNR falls below some threshold, we are primarily concerned with regions of Fourier space to which few photons scatter. For non-isotropically scattering samples, such as crystals, it is the signal between Bragg peaks that will define q_c. Thus, equation (8) holds even for scattering from crystals.

APPENDIX B
Crystalline discontinuities

For crystalline materials it is possible to determine when the expected resolution will become discontinuous as a function of dose. Since it is the regions of low SNR that determine the resolution, the cutoff frequency [equation (8)] will jump across regions of high SNR, such as Bragg peaks. Far from a Bragg peak, the asymptotic form of the scattered intensity can be used. Thus, the (000) contribution to the azimuthally averaged intensity is then

$$\left\langle I_0\right\rangle_q \propto\; Z^2/q^4, \quad (9)$$

where the unit-cell structure factor, $F(q = 0) = Z$, is the sum of atomic numbers in the unit cell. It is not important to know the absolute intensity, since only the ratio of two Bragg peak intensities will later be used. The contribution from any other Bragg peak at $q_b \neq 0$ to the azimuthally averaged intensity has the asymptotic form

$$\left\langle I_b\right\rangle_q \propto\; \frac{m_b|F(q_b)|^2}{4qq_b(q - q_b)^2}, \quad (10)$$

where m_b is the peak multiplicity, given by the number of symmetry-equivalent reflections. The first discontinuity will be due to a jump across the first non-forbidden Bragg peak, scaled by an additional factor of inverse wavevector due to rotation in three dimensions as seen in equation (2). The start of this jump is determined by the minima in inter-peak intensity and is given by

$$\frac{\mathrm{d}}{\mathrm{d}q}\left[\frac{1}{q}\left(\left\langle I_0\right\rangle_q + \left\langle I_b\right\rangle_q\right)\right]\Big|_{q_1} = 0.$$

Using equations (9) and (10) a quadratic expression is obtained,

$$10\rho_{0,b}(q_b - q_1)^3 q_b = q_1^3(2q_1 - q_b), \quad (11)$$

where $\rho_{0,b} = Z^2/m_b|F(q_b)|^2$. This has four roots, one of which is the correct turnover point between $q = 0$ and q_b. Although the analytic roots can be written, they are generally far too complicated to be used directly. The recommendation is to find the numeric root. Nonetheless, an approximate analytic root can be found by looking near $q_b/2$, half way between the two Bragg peaks. Using a first-order Taylor series expansion, the approximate turnover point is given by

$$q_1 \approx \frac{q_b}{2}\left(\frac{40\rho_{0,b} + 1}{30\rho_{0,b} + 1}\right), \quad (12)$$

which is valid when $\rho_{0,b} \simeq 10^{-1}$. The jump ends when the same intensity is reached on the other side of the first Bragg peak. Thus, if this Bragg peak is sufficiently separated from others, such that a low-intensity region exists directly after the peak at q_b, then the end point is given by

$$q_2^2(q_2 - q_b)^2 = q_1^2(q_b - q_1)^2/\alpha, \tag{13}$$

where $\alpha = 1 + 4\rho_{0,b}[q_b(q_b - q_1)^2/q_1^3]$. This quadratic equation has analytic roots, but once again it is simpler to calculate the solution numerically. It is also possible to estimate the end point by looking for a root near $2q_b - q_1$ which has the same separation as the start point to the Bragg center. By performing a first-order Taylor series expansion, the end point is given by

$$\begin{aligned} q_2 &\approx 2q_b - q_1 - \frac{(q_b - q_1)\left[(2q_b - q_1)^2 - q_1^2/\alpha\right]}{2(2q_b - q_1)(3q_b - 2q_1)} \\ &\approx \frac{18}{11}q_b - \frac{5}{8}q_1, \end{aligned} \tag{14}$$

where the second approximations assumes the intensity at q_1 is dominated by $\langle I_b \rangle_{q_1}$. By following the same method, the jumps across higher Bragg peaks can also be determined, but are not derived here.

Acknowledgements

This work was supported by US Department of Energy, Office of Science, Office of Basic Energy Sciences, under Contract DE-SC0001805.

References

Abbey, B., Whitehead, L. W., Quiney, H. M., Vine, D. J., Cadenazzi, G. A., Henderson, C. A., Nugent, K. A., Balaur, E., Putkunz, C. T., Peele, A. G. J. W. & McNulty, I. (2011). *Nat. Photon.* **5**, 420–424.

Als-Nielsen, J. & McMorrow, D. (2011). *Elements of Modern X-ray Physics*, 2nd ed. New York: John Wiley and Sons.

Averbuch, A., Coifman, R., Donoho, D., Elad, M. & Israeli, M. (2006). *Appl. Comput. Harmon. Anal.* **21**, 145–167.

Bates, R. (1984). *Comput. Vis. Graph. Image Process.* **25**, 205–217.

Bell, A. M. T., Henderson, C. M. B., Wendlandt, R. F. & Harrison, W. J. (2009). *Acta Cryst.* E**65**, i16–i17.

Bilderback, D. H., Brock, J. D., Dale, D. S., Finkelstein, K. D., Pfeifer, M. A. & Gruner, S. M. (2010). *Nat. Photon.* **12**, 035011.

Bragg, W. L. (1913). *Proc. R. Soc. London A*, **89**(610), 248–277.

Burgess, A. E. (1999). *J. Opt. Soc. Am. A*, **16**, 633–646.

Chapman, H. N., Barty, A., Marchesini, S., Noy, A., Hau-Riege, S. P., Cui, C., Howells, M. R., Rosen, R., He, H., Spence, J. C. H., Weierstall, U., Beetz, T., Jacobsen, C. & Shapiro, D. (2006). *J. Opt. Soc. Am. A*, **23**, 1179–1200.

Crimmins, T. R., Fienup, J. R. & Thelen, B. J. (1990). *J. Opt. Soc. Am. A*, **7**, 3–13.

Crowfoot, D., Bunn, C. W., Rogers-Low, B. W. & Turner-Jones, A. (1949). *Chemistry of Penicillin*, edited by H. T. Clarke, J. R. Johnson and R. Robinson, pp. 310–367. Princeton University Press.

Elser, V. (2003). *J. Opt. Soc. Am. A*, **20**, 40–55.

Eriksson, M., Lindgren, L.-J., Sjöström, M., Wallén, E., Rivkin, L. & Streun, A. (2008). *Nucl. Instrum. Methods Phys. Res. A*, **587**, 221–226.

Fenn, M., Kunis, S. & Potts, D. (2007). *Appl. Comput. Harmon. Anal.* **22**, 257–263.

Fienup, J. R. (1980). *Opt. Eng.* **19**, 193297.

Fienup, J. R. (1982). *Appl. Opt.* **21**, 2758–2769.

Fienup, J. R., Thelen, B. J., Reiley, M. F. & Paxman, R. G. (1997). *Proc. SPIE*, **3170**, 88–96.

Foster, A. S., Barth, C., Shluger, A. L. & Reichling, M. (2001). *Phys. Rev. Lett.* **86**, 2373–2376.

Hegerl, R. & Hoppe, W. (1976). *Z. Naturforsch. A*, **31**, 1717–1721.

Holt, M., Wu, Z., Hong, H., Zschack, P., Jemian, P., Tischler, J., Chen, H. & Chiang, T.-C. (1999). *Phys. Rev. Lett.* **83**, 3317–3319.

Howells, M., Beetz, T., Chapman, H., Cui, C., Holton, J., Jacobsen, C., Kirz, J., Lima, E., Marchesini, S., Miao, H., Sayre, D., Shapiro, D., Spence, J. & Starodub, D. (2009). *J. Electron Spectrosc. Relat. Phenom.* **170**(13), 4–12.

Jette, E. R. & Foote, F. (1935). *J. Chem. Phys.* **3**, 605–616.

Johansson, G. A., Tyliszczak, T., Mitchell, G. E., Keefe, M. H. & Hitchcock, A. P. (2007). *J. Synchrotron Rad.* **14**, 395–402.

Kim, J. W., Manna, S., Dietze, S. H., Ulvestad, A., Harder, R., Fohtung, E., Fullerton, E. E. & Shpyrko, O. G. (2014). *Appl. Phys. Lett.* **105**, 173108–173112.

Lee, C.-Y., Stachurski, Z. H. & Richard Welberry, T. (2010). *Acta Mater.* **58**, 615–625.

Marchesini, S., Chapman, H., Hau-Riege, S., London, R., Szoke, A., He, H., Howells, M., Padmore, H., Rosen, R., Spence, J. & Weierstall, U. (2003*a*). *Opt. Express*, **11**, 2344–2353.

Marchesini, S., He, H., Chapman, H. N., Hau-Riege, S. P., Noy, A., Howells, M. R., Weierstall, U. & Spence, J. C. H. (2003*b*). *Phys. Rev. B*, **68**, 140101.

McEwen, B. F., Downing, K. H. & Glaeser, R. M. (1995). *Ultramicroscopy*, **60**, 357–373.

Miao, J., Charalambous, P., Kirz, J. & Sayre, D. (1999). *Nature (London)*, **400**, 342–344.

Miao, J., Chen, C.-C., Song, C., Nishino, Y., Kohmura, Y., Ishikawa, T., Ramunno-Johnson, D., Lee, T.-K. & Risbud, S. H. (2006). *Phys. Rev. Lett.* **97**, 215503.

Miao, J., Ishikawa, T., Robinson, I. K. & Murnane, M. M. (2015). *Science*, **348**, 530–535.

Miao, J., Sayre, D. & Chapman, H. N. (1998). *J. Opt. Soc. Am. A*, **15**, 1662–1669.

Neutze, R., Wouts, R., van der Spoel, D., Weckert, E. & Hajdu, J. (2000). *Nature (London)*, **406**, 752–757.

Newton, M. C., Leake, S. J., Harder, R. & Robinson, I. K. (2009). *Nat. Mater.* **9**, 120–124.

Nyquist, H. (1928). *Trans. Am. Inst. Electr. Eng.* **47**, 617–644 [Reprinted in *Proc. IEEE*, (2002). **90**, 280].

Peng, L.-M., Ren, G., Dudarev, S. L. & Whelan, M. J. (1996). *Acta Cryst.* A**52**, 456–470.

Peterson, W., Birdsall, T. & Fox, W. (1954). *Trans. IRE Prof. Group Inf. Theory*, **4**, 171–212.

Quiney, H. (2010). *J. Mod. Opt.* **57**, 1109–1149.

Rasche, V., Proksa, R., Sinkus, R., Börnert, P. & Eggers, H. (1999). *IEEE Trans. Med. Imaging*, **18**, 385–392.

Rose, A. (1948). *J. Opt. Soc. Am.* **38**, 196–208.

Schweinfest, R., Köstlmeier, S., Ernst, F., Elsäser, C., Wagner, T. & Finnis, M. W. (2001). *Philos. Mag. A*, **81**, 927–955.

Shannon, C. E. (1949). *Proc. IRE*, **37**, 10–21 [Reprinted in *Proc. IEEE*, (1998). **86**, 447–457].

Shen, Q., Bazarov, I. & Thibault, P. (2004). *J. Synchrotron Rad.* **11**, 432–438.

Shirage, P., Kihou, K., Lee, C., Kito, H., Eisaki, H. & Iyo, A. (2013). *Physica C*, **484**, 12–15.

Sinha, S. K., Tolan, M. & Gibaud, A. (1998). *Phys. Rev. B*, **57**, 2740–2758.

Song, C., Ramunno-Johnson, D., Nishino, Y., Kohmura, Y., Ishikawa, T., Chen, C.-C., Lee, T.-K. & Miao, J. (2007). *Phys. Rev. B*, **75**, 012102.

Starodub, D., Rez, P., Hembree, G., Howells, M., Shapiro, D., Chapman, H. N., Fromme, P., Schmidt, K., Weierstall, U., Doak, R. B. & Spence, J. C. H. (2008). *J. Synchrotron Rad.* **15**, 62–73.

Stinton, G. W. & Evans, J. S. O. (2007). *J. Appl. Cryst.* **40**, 87–95.

Takahashi, Y., Nishino, Y., Tsutsumi, R., Kubo, H., Furukawa, H., Mimura, H., Matsuyama, S., Zettsu, N., Matsubara, E., Ishikawa, T. & Yamauchi, K. (2009). *Phys. Rev. B*, **80**, 054103.

Thibault, P., Elser, V., Jacobsen, C., Shapiro, D. & Sayre, D. (2006). *Acta Cryst.* A**62**, 248–261.

Thibault, P. & Menzel, A. (2013). *Nature (London)*, **494**, 68–71.

Tripathi, A., Mohanty, J., Dietze, S. H., Shpyrko, O. G., Shipton, E., Fullerton, E. E., Kim, S. S. & McNulty, I. (2011). *Proc. Natl. Acad. Sci. USA*, **108**, 13393–13398.
Ulvestad, A., Cho, H. M., Harder, R., Kim, J. W., Dietze, S. H., Fohtung, E., Meng, Y. S. & Shpyrko, O. G. (2014). *Appl. Phys. Lett.* **104**, 073108.
Waasmaier, D. & Kirfel, A. (1995). *Acta Cryst.* A**51**, 416–431.
Watson, J. D. & Crick, F. H. C. (1953). *Nature (London)*, **171**, 737–738.
Weiß, D., Schneider, G., Niemann, B., Guttmann, P., Rudolph, D. & Schmahl, G. (2000). *Ultramicroscopy*, **84**(34), 185–197.
Withers, P. J. (2007). *Mater. Today*, **10**, 26–34.
Wu, Z., Hong, H., Aburano, R., Zschack, P., Jemian, P., Tischler, J., Chen, H., Luh, D.-A. & Chiang, T.-C. (1999). *Phys. Rev. B*, **59**, 3283–3286.